Encoding Abrupt and Uniform Dopant Profiles in Vapor–Liquid–Solid Nanowires by Suppressing the Reservoir Effect of the Liquid Catalyst

Joseph D. Christesen,[†] Christopher W. Pinion,[†] Xing Zhang,[†] James R. McBride,[*,‡] and James F. Cahoon[*,†]

[†]Department of Chemistry, University of North Carolina at Chapel Hill, Chapel Hill, North Carolina 27599-3290, United States and [‡]Vanderbilt Institute of Nanoscale Science and Engineering, Vanderbilt University, Nashville, Tennessee 37235, United States

ABSTRACT Semiconductor nanowires (NWs) are often synthesized by the vapor–liquid–solid (VLS) mechanism, a process in which a liquid droplet—supplied with precursors in the vapor phase—catalyzes the growth of a solid, crystalline NW. By changing the supply of precursors, the NW composition can be altered as it grows to create axial heterostructures, which are applicable to a range of technologies. The abruptness of the heterojunction is mediated by the liquid catalyst, which can act as a reservoir of material and impose a lower limit on the junction width. Here, we demonstrate that this "reservoir effect" is not a fundamental limitation and can be suppressed by selection of specific VLS reaction conditions. For Au-catalyzed Si NWs doped with P, we evaluate dopant profiles under a variety of synthetic conditions using a combination of elemental imaging with energy-dispersive X-ray spectroscopy and dopant-dependent wet-chemical etching. We observe a diameter-dependent reservoir effect under most conditions. However, at sufficiently slow NW growth rates (≤250 nm/min) and low reactor pressures (≤40 Torr), the dopant profiles are diameter independent and radially uniform with abrupt, sub-10 nm axial transitions. A kinetic model of NW doping, including the microscopic processes of (1) P incorporation into the liquid catalyst, (2) P evaporation from the catalyst, and (3) P crystallization in the Si NW, quantitatively explains the results and shows that suppression of the reservoir effect can be achieved when P evaporation is much faster than P crystallization. We expect similar reaction conditions can be developed for other NW systems and will facilitate the development of NW-based technologies that require uniform and abrupt heterostructures.

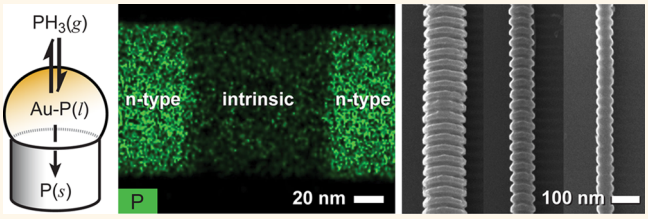

KEYWORDS: silicon nanowire · vapor–liquid–solid mechanism · reservoir effect · phosphorus doping · wet-chemical etching

Semiconductor nanowires (NWs) have been developed as a bottom-up technological platform for a variety of electronic,[1,2] photonic,[3–5] and photovoltaic[6–9] devices. Several of these technologies require modulation of the NW composition along the growth axis to form heterostructures that are required for specific device functions. For instance, NWs with n-type/intrinsic or p-type/intrinsic junctions have been explored as field-effect transistors, enabling both electronic devices[2,10,11] and sensors.[12–14] Similarly, NWs with p-type/n-type junctions have been synthesized in Si,[14–18] GaAs,[17] InP,[19] *etc.*, and used for photovoltaic devices,[15–17] avalanche photodetectors,[18] Esaki diodes,[20,21] and light-emitting diodes.[22,23] Nevertheless, it is generally believed that heterostructures formed by the vapor–liquid–solid (VLS) process will have broad junctions with a width approximately equal to the wire diameter.[24–26] Considering the wide-ranging applications for NW heterostructures, it is increasingly important to understand the microscopic kinetic processes that govern heterostructure formation and to develop methods that overcome the limitations on the transition width.

During the VLS process (Figure 1A),[27,28] a liquid droplet composed of metal and semiconductor is formed by supplying a vapor-phase semiconductor precursor (*e.g.*, SiH_4 and GeH_4) to a metal nanoparticle and raising the local temperature above the eutectic point for the two materials. When the liquid droplet is supersaturated, which typically requires semiconductor weight

* Address correspondence to james.r.mcbride@vanderbilt.edu, jfcahoon@unc.edu.

Received for review September 23, 2014 and accepted November 1, 2014.

Published online November 02, 2014
10.1021/nn505404y

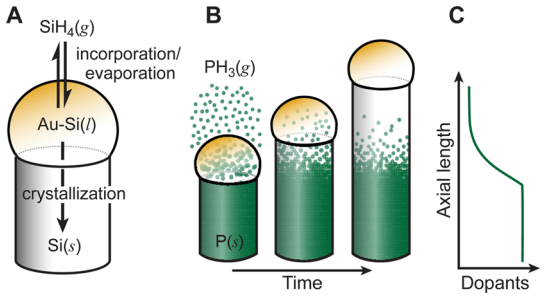

Figure 1. VLS NW growth and the reservoir effect. (A) Illustration of the key kinetic processes during Si NW growth: incorporation, evaporation, and crystallization. (B) Schematic of the reservoir effect, showing (left) a supply of P dopant precursor in the gas phase followed by (middle) removal of the gas-phase precursor with retention of P by the liquid catalyst and (right) subsequent depletion of P dopants from the liquid catalyst. (C) Plot of dopant concentration along the axial length of the NW.

fractions of 10−50%,[29,30] a NW will nucleate and grow. Heterostructures are formed by altering the supply of vapor-phase precursors during VLS growth. However, the liquid droplet can act as a reservoir of material even after a precursor has been removed, causing the heterojunction to be broadened by a phenomena termed the "reservoir effect", as illustrated in Figure 1B,C.[31−33] This effect has been observed for heterostructures involving a change in dopants (*e.g.*, P-doped Si[34] and Si-doped GaAs[35]) and structures involving a change in semiconductor (*e.g.*, Si/Ge[25,36,37] and GaAs/InAs[38,39]).

For group IV NWs, transition widths comparable to the wire diameter have been observed for P dopant transitions[34] as well as junctions between Si and Ge.[25,36,37] Several strategies to mitigate this effect have been developed. For example, metal catalysts with a lower solubility of semiconductor in the liquid, such as an $Au_{1-x}Ga_x$ alloy,[24] can shorten the transition width. Another alternative is to forego the VLS mechanism in favor of a vapor−solid−solid (VSS) mechanism, in which the metal catalyst is solid and has little to no solubility with the semiconductor.[29,31] The VSS growth process has been successfully demonstrated for dopant transitions in Au-catalyzed NWs[12] and for Si/Ge transitions in AuAl-catalyzed NWs.[31] Although VSS growth has been shown to produce near-atomic compositional transitions, the growth rate is slow, preventing application for many devices. For III−V NWs, the reservoir effect has been observed for heterostructures involving a change in dopant[26] and a change in the group III material.[25] However, the effect is generally not observed for a change in the group V material, which has been attributed to the low solubility of group V elements in the liquid catalyst.[24] For structures in which the group III material is changed, methods such as pulsing the group III precursor have improved the transition width, resulting, for example, in sharper InAs/GaAs transitions.[33] In this case, it is believed that Ga reduces the solubility of In in the metal catalyst to reduce the reservoir effect; however, a general strategy for suppression of the effect has yet to be developed.

Here, we investigate the uniformity and abruptness of P dopant transitions in Si NWs grown by the VLS mechanism with Au catalysts. Transitions between n-type and intrinsic sections of the Si NW are quantitatively evaluated by elemental mapping with ∼1 nm spatial resolution using energy-dispersive X-ray spectroscopy (EDS) in a scanning transmission electron microscope (STEM). Previous attempts to quantitatively resolve dopants in NWs have been hindered by low signal-to-noise ratios and long acquisition times;[12,40] however, this problem is mitigated by the simultaneous X-ray detection of four solid-state detectors in conjunction with the high-brightness Schottky-type field-emission gun of the STEM used in this work (FEI Tecnai Osiris; see Methods). The transitions are also evaluated by wet-chemical etching of doped nanowires using the recently reported ENGRAVE (Encoded Nanowire GRowth and Appearance through VLS and Etching) process.[41] We develop a kinetic model of NW doping, which includes the microscopic processes of (1) P incorporation into the liquid catalyst, (2) P evaporation from the catalyst, and (3) P crystallization in the Si NW. We find a VLS growth regime in which the reservoir effect is fully suppressed because the rate of P evaporation greatly exceeds the rate of P crystallization. In this regime, NWs with diameters from 50 to 150 nm are encoded with abrupt and uniform dopant transitions, as verified by high-resolution morphologies encoded through the ENGRAVE process. The results suggest that the reservoir effect can be suppressed for any VLS growth system in which the rate of liquid−vapor equilibrium can greatly exceed the rate of NW growth.

RESULTS

Si NWs were synthesized in a hot-wall chemical vapor deposition (CVD) reactor at 420 °C and a range of total pressures (20−80 Torr) using SiH_4 and PH_3 as the Si and P precursors, respectively, and H_2 as the carrier gas (see Methods for further details). Calibration of the NW growth rate, as described previously,[28] enabled the growth of n-type and intrinsic sections with precise axial lengths by modulating the flow of PH_3 for specific time intervals. EDS images in Figure 2A for NWs grown at 20 Torr show strong P signals from the doped sections and relatively abrupt transitions at the n-type/intrinsic interfaces, which will be analyzed in detail below. Wet-chemical etching of the NWs in KOH solution leads to diameter modulation along the axis, as shown by the scanning electron microscopy (SEM) image in Figure 2A. The large diameter segments correspond to the n-type sections, which act as an etch stop as described previously for the ENGRAVE process.[41] As shown in Figure 2B, the EDS and SEM diameter measurements directly correlate with the PH_3

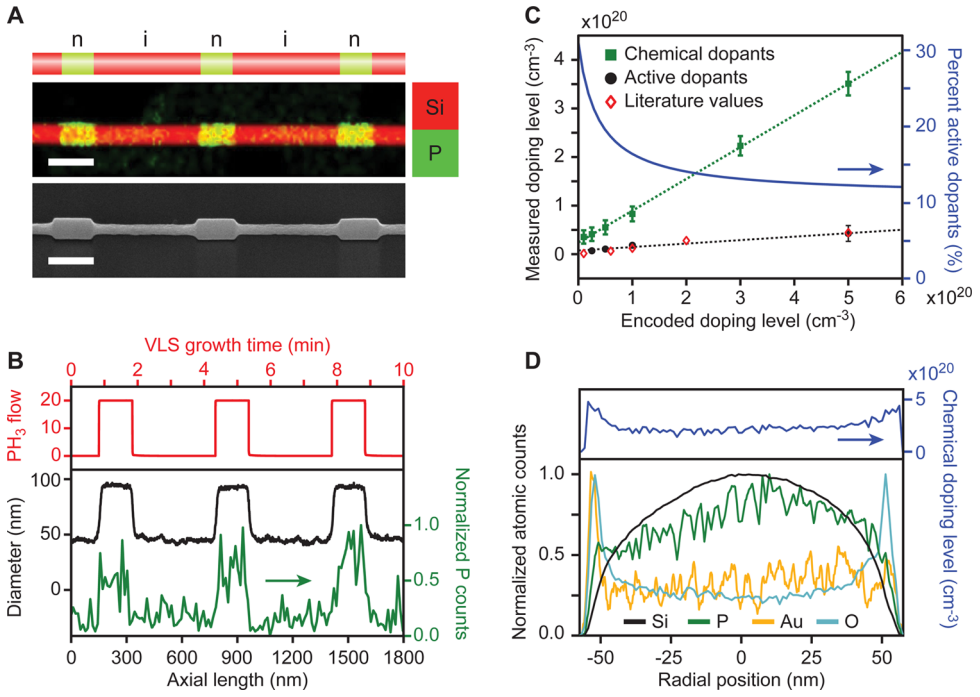

Figure 2. Characterization of P doping in VLS-grown Si NWs. (A) Top: Schematic of a Si NW with intrinsic (i) sections depicted in red and P-doped, n-type (n) sections depicted in green. Middle: STEM EDS image of a Si NW showing P counts in green and Si counts in red; scale bar, 200 nm. Bottom: SEM image of Si NW after wet-chemical KOH etching; scale bar, 200 nm. (B) Top: PH_3 flow profile (in units of standard cubic centimeters per minute, sccm) during VLS growth of the NWs shown in panel A. Bottom: Diameter profile (black curve and left-hand axis) derived from the SEM image in panel A and P signal (green curve and right-hand axis) derived from the EDS image in panel A. (C) Active doping level from resistivity measurements (black circles) and chemical doping level from EDS measurements (green squares) as a function of the encoded doping level, which corresponds to the gas-phase ratio of P to Si. Literature values for active doping level from ref 42 are shown as red diamonds, and dashed lines represent linear fits to the data. Blue line and right-hand axis show the percentage of active dopants based on the ratio of active to chemical doping level. (D) Top: Chemical doping level as a function of radial position for a NW with encoded doping level of 5×10^{20} cm^{-3}. Bottom: Normalized EDS signals as a function of radial position for Si (black), P (green), Au (gold), and O (light blue). Chemical doping level in the top panel is determined by the ratio of the P to Si EDS signals. All NWs shown in panels A–D were grown with a SiH_4 partial pressure of 0.4 Torr and a total pressure of 40 Torr.

flow profile. Both measurements reflect dopant incorporation in the wire and are used to evaluate the abruptness of the n-type/intrinsic junctions.

The doping level of the n-type sections was evaluated using both quantitative EDS signal analysis and single-NW resistivity measurements to determine the chemical doping level (*i.e.*, the density of P atoms) and the active doping level (*i.e.*, the density of ionized P atoms), respectively. The nominal encoded doping level, as determined by the vapor-phase ratio of PH_3 to SiH_4, ranged from 5×10^{20} cm^{-3} (1:100 PH_3:SiH_4) to 1×10^{19} cm^{-3} (1:5000 PH_3:SiH_4). As shown in Figure 2C, EDS analysis (see Figure S1 for a representative fit of an EDS spectrum) yielded chemical doping levels that were ~60% of the nominal encoded level. Resistivity measurements, however, yielded active doping levels (see Figure 2C) that were ~10% of the encoded doping level (see Figure S2, Table S1, and Methods for details on the resistivity measurements). The resistivity measurements are in good agreement with previous reports on NW doping with PH_3.[42−44] However, a comparison of the chemical and active doping level measurements (right-hand axis of Figure 2C) indicates that less than 13% of the dopants in the NW are ionized and thus active for the highest doping levels, and less than 30% are active at the lowest doping level. Although donor deactivation has been reported in silicon nanostructures as a result of dielectric mismatch with the surrounding medium,[45] the magnitude of the deactivation determined here for NWs that are ~100 nm in diameter is not well explained by this effect. Instead, the deactivation is likely due to lattice distortions and/or the formation of P dimers at the relatively low temperature (420 °C) used for VLS growth.[46] The possibility to activate a larger fraction of the dopants through postgrowth thermal annealing will be investigated in future studies.

The uniformity of doping in the n-type sections was evaluated with radial EDS scans for Si, P, Au, and O, as shown in Figure 2D (see Figure S3 for additional details on the radial scan). A plot of chemical doping level *vs* radial position (see right-hand axis of Figure 2D) shows an increase in the P concentration toward the outer radial positions of the NW. An increasing P concentration toward the surface of the NW is in good agreement with previous studies, which have reported a high surface concentration of P due to vapor−solid (VS) overcoating[34,47] or from other surface-related effects.[48]

Here, the extent of VS overcoating is minimized by the use of a relatively low VLS growth temperature, 420 °C, which suppresses SiH_4 decomposition on the NW sidewalls (see Figure S4). In addition, the region of higher doping corresponds to the region with higher O counts because of a native oxide on the wire surface. As a result, we expect this region is readily removed when wires are wet-chemically etched to remove the oxide, so electronic devices and the ENGRAVE process[41] should not be substantially affected by this layer. We also note that the radial dependence of the P signal may be overestimated as a result of spectral overlap of an X-ray peak from Au with the peak from P because the wires also show aggregation of Au on the wire surface (see Figure S3).

High-resolution EDS and SEM imaging, as shown in Figure 3A and B, was used to quantify the abruptness of the n-type/intrinsic transitions. Line profiles generated from vertical sectioning of the images are displayed in Figure 3C. These profiles were fit to single-exponential functions convoluted with a Gaussian (eq S1) to extract the characteristic decay length, λ, of the transitions. The Gaussian convolution represents experimental broadening due to mass transport of etchant for SEM images and represents the finite beam size for EDS imaging (see Methods for details). The fits (dashed lines in Figure 3C) provide a reasonable representation of the transition widths, and the SEM data are also corrected (see Methods) for the exponential relationship[41,49] between the etch rate and encoded doping level. This analysis yields a measured transition length of 4 and 5 nm from the EDS and SEM data, respectively, in Figure 3C, demonstrating the good agreement between these two methods. The measured transition widths are substantially shorter than previous reports,[25,26] and we develop below a kinetic model of NW doping in order to interpret the results. Note that for n-type/intrinsic/n-type sections, there is no apparent dependence of the transition width on intrinsic segment length. Diameter profiles and SEM images in Figure 3D and E show the same profile for intrinsic segments 10 to 200 nm in length; however, the smaller segments are etched to a lesser extent presumably because mass transport to the etched region is hindered by the small dimensions. In addition, the first transition region (n-type/intrinsic) shows the same abruptness (<10 nm) as the second transition (intrinsic/n-type).

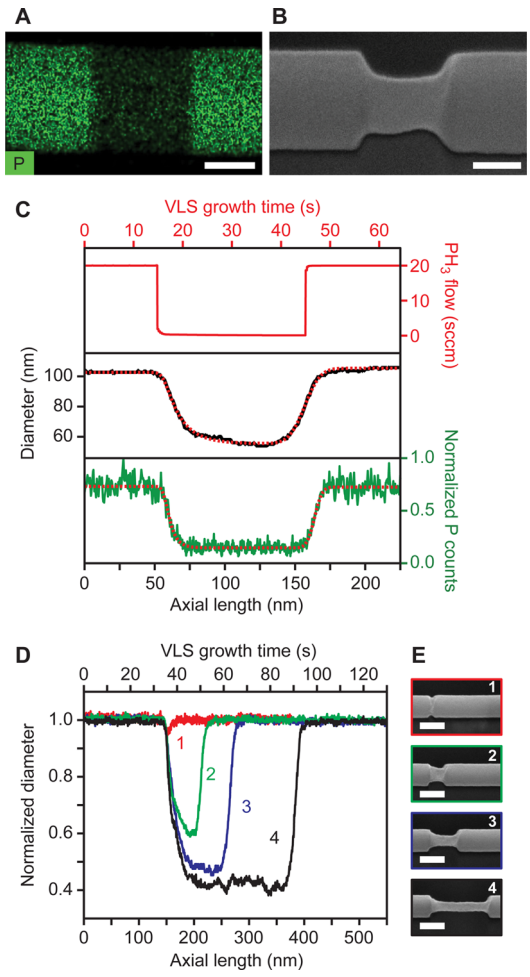

Figure 3. Evaluating the abruptness of P dopant profiles in Si NWs. (A) EDS image, showing P counts in green, for an n-type/intrinsic/n-type wire with a ~100 nm intrinsic section; scale bar, 50 nm. (B) SEM image of a NW, grown under the same conditions as in panel A, after wet-chemical KOH etching; scale bar, 50 nm. (C) Top: PH_3 flow profile (red curve) in units of sccm for the n-type/intrinsic/n-type sections shown in panels A and B. Middle: Diameter profile (black curve) derived from the SEM image in panel B and best fit (red dashed line) to eq S1. Bottom: P counts (green curve) derived from the EDS image in panel A and best fit (red dashed line) to eq S1. (D) Normalized diameter profiles for etched segments along a single NW corresponding to intrinsic segments grown for (1) 6 s (red), (2) 15 s (green), (3) 30 s (blue), and (4) 60 s (black). (E) SEM images of the four segments corresponding to the diameter profiles in panel D. All NWs shown in panels A–E were grown with a SiH_4 partial pressure of 0.4 Torr and a total pressure of 40 Torr.

KINETIC MODELING AND ANALYSIS

We analyze P dopant incorporation in Si NWs using the three microscopic kinetic processes depicted in Figure 4A: P incorporation, P evaporation, and P crystallization.[50] By analyzing the rate equations, we can construct a kinetic model of NW growth that predicts the transition width for a set of physically reasonable assumptions. First, we assume the engineering of the CVD system, such as switching speed of the mass flow controllers and rate of gas exchange in the system, has no influence on the observed transition width, which is verified by control growth studies (see Figure S5). Second, we assume the NW growth rate is independent of the concentration of vapor-phase PH_3 or P dissolved in the liquid, which is supported by our previous studies of VLS growth kinetics.[28] Third, we assume that, prior to a transition, the dopant has reached a steady-state concentration and is uniformly

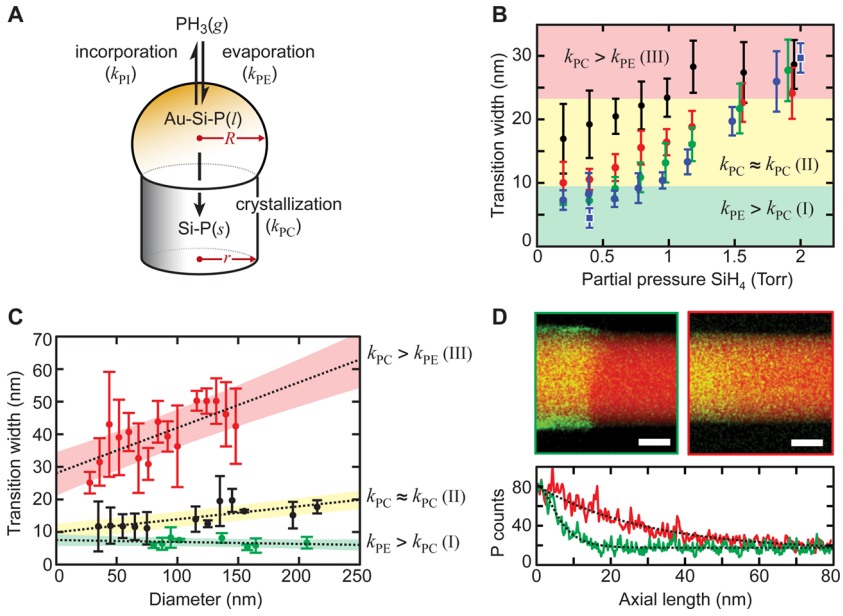

Figure 4. Influence of NW growth rate and diameter on the abruptness of n-type/intrinsic dopant heterostructures. (A) Illustration of the key processes for describing the time-dependent P concentration in the catalyst and NW: incorporation, evaporation, and crystallization. (B) Plot of transition width relative to partial pressure of SiH_4 for 20 (blue), 40 (green), 60 (red), and 80 (black) Torr total reactor pressure. Blue square data points outlined in white represent transition widths derived from EDS data in panel D. (C) Plot of transition width *vs* diameter for NWs grown at a SiH_4 partial pressure of 0.4 Torr and a total reactor pressure of 20 (green) or 80 (black) Torr, as well as a SiH_4 partial pressure of 2.0 Torr (red) and a total reactor pressure of 20 Torr. Black dashed lines are the best linear fits to each data set, and shaded areas represent one standard deviation error in the fit. (D) EDS images (top) and plot of relative atomic counts *vs* axial length (bottom) for NWs grown at a SiH_4 partial pressure of 0.4 Torr (left, green) and 2.0 Torr (right, red) at a total reactor pressure of 20 Torr, with growth rates of ~100 and ~500 nm/min, respectively. The wire grown at a SiH_4 partial pressure of 0.4 Torr shows higher P counts on the edge as a result of higher Au concentration on the surface (see Figure S3). The transition widths from these images are plotted in panel B as blue squares with a white outline.

distributed in the liquid catalyst, which is confirmed by the homogeneity of the P signal in Figure 2D. Note that the kinetic analysis below is used to interpret the transition width of n-type/intrinsic transitions but not intrinsic/n-type transitions. For the latter transitions, in which the n-type region is grown after the intrinsic region, an abrupt, sub-10 nm transition is consistently observed. We attribute this abruptness to a uniformly high rate of P incorporation under all VLS growth conditions.

For the kinetic analysis of n-type/intrinsic transitions, we define the doping level, N_d, as the ratio of the volumetric rate of P crystallization to volumetric rate of Si crystallization:

$$N_d = \frac{k_{PC}C_{P(l)}\pi r^2\Omega_P}{k_{SiC}C_{Si(l)}\pi r^2\Omega_{Si}} \approx \frac{k_{PC}C_{P(l)}}{k_{SiC}C_{Si(l)}} \quad (1)$$

where k_{PC} is the rate constant for P crystallization (units of nm/s), k_{SiC} is the rate constant for Si crystallization (units of nm/s), $C_{P(l)}$ is the concentration of P in the liquid catalyst, $C_{Si(l)}$ is the concentration of Si in the liquid catalyst, r is the radius of the solid NW, and Ω_{Si} and Ω_P are the Si and P volumes per atom, respectively. We also assume $\Omega_{Si} \approx \Omega_P$, leading to the simplification shown on the right-hand side of eq 1. During an n-type/intrinsic transition, the dopant width is dictated by the time-dependence of $C_{P(l)}$, which decreases as a result of P crystallization and evaporation as

$$\frac{dC_{P(l)}}{dt} = -k_{PE}C_{P(l)}\frac{S}{V} - k_{PC}C_{P(l)}\frac{A}{V} \quad (2)$$

where k_{PE} is the rate constant for P evaporation (units of nm/s), S is the liquid−vapor interfacial surface area, V is the volume of the liquid catalyst, and A is the cross-sectional area of the NW (equal to πr^2). Solving eq 2 for $C_{P(l)}$ and inserting the result into eq 1 assuming a partial sphere geometry for the liquid catalyst yields

$$N_d(t) = \frac{k_{PC}C_{o,P(l)}}{k_{SiC}C_{Si(l)}}\exp\left(\frac{-3\left(2Rk_{PE} + \frac{r^2}{R+\alpha}k_{PC}\right)}{(R+\alpha)(2R-\alpha)}t\right) \quad (3)$$

where $C_{o,P(l)}$ is the initial concentration of P in the metal catalyst, R is the liquid catalyst diameter, α is $(R^2 - r^2)^{1/2}$, and t is the total amount of time after the P precursor has been turned off. The growth rate, G, of the NW, as developed previously,[28] is

$$G = L/t = \Omega_{Si}k_{SiC}C_{Si(l)} \quad (4)$$

where L is the length of the segment grown in time t. Note that the rate constant, k_{SiC}, can have a dependence on the supersaturation of the liquid droplet and

thus on the supply of Si precursor (*e.g.*, partial pressure of SiH_4).[28,51] Rearranging eq 4 and substituting for t in eq 3 yields

$$N_d(L) = \frac{k_{PC}C_{o,P(l)}}{k_{SiC}C_{Si(l)}}\exp\left(\frac{-3\left(2Rk_{PE}+\frac{r^2}{R+\alpha}k_{PC}\right)}{(R+\alpha)(2R-\alpha)k_{SiC}\varphi_{Si}}L\right)$$
$$= \frac{k_{PC}C_{o,P(l)}}{k_{SiC}C_{Si(l)}}\exp(-L/\lambda) \quad (5)$$

where $\phi_{Si} = \Omega_{Si}C_{Si(l)}$ is the volume fraction of Si in the liquid catalyst, and the transition width, λ, is defined as

$$\lambda = \frac{(R+\alpha)(2R-\alpha)k_{SiC}\varphi_{Si}}{3\left(2Rk_{PE}+\frac{r^2}{R+\alpha}k_{PC}\right)} \approx \frac{2k_{SiC}\varphi_{Si}}{3(2k_{PE}+k_{PC})}R \quad (6)$$

If the catalyst droplet is assumed to be a hemisphere, then $R = r$, α is zero, and λ is linearly dependent on the NW radius, as shown on the right-hand side of eq 6.[25,26] However, λ is also dependent on the rate constants k_{SiC}, k_{PC}, and k_{PE}, so we consider several limiting values of these constants to understand the presence—or absence—of the reservoir effect under a variety of synthetic conditions.

We assume that k_{SiC} is nonzero and separately consider the limits of eq 6 if P evaporation is much faster than P crystallization (*i.e.*, $k_{PE} \gg k_{PC}$) or if P crystallization is much faster than P evaporation (*i.e.*, $k_{PC} \gg k_{PE}$). In the first limit, eq 6 becomes

$$\lambda \approx \frac{k_{SiC}\varphi_{Si}}{3k_{PE}}R, \text{ for } k_{PE} >> k_{PC} \quad (7)$$

In this limit, λ goes to zero if the rate constant of P evaporation is much greater than the rate constant for Si crystallization (*i.e.*, $k_{PE} \gg k_{SiC}$), causing the reservoir effect to be fully suppressed. In the second limit, eq 6 becomes

$$\lambda \approx \frac{2k_{SiC}\varphi_{Si}}{3k_{PC}}R = \frac{2}{3}\beta\varphi_{Si}R, \text{ for } k_{PC} >> k_{PE} \quad (8)$$

where $\beta = k_{SiC}/k_{PC}$ is the segregation coefficient[50] for crystallization of Si and P in the NW (*i.e.*, the ratio of P concentration in the liquid to P concentration in the NW). In this limit, the transition width is linearly dependent on the radius, R, and there is no regime (for VLS growth of Si with Au catalysts) in which the reservoir effect can be suppressed.

To experimentally delineate the different regimes in eqs 7 and 8, we systematically varied NW growth conditions—including NW diameter, growth rate (*i.e.*, SiH_4 partial pressure), and the total CVD reactor pressure—and observed the effect on the NW transition width as measured by wet-chemical etching (see Figure 4B and C). Three distinct regions (I, II, and III) were identified. First, at low total pressures (<40 Torr) and relatively low growth rates (<300 nm/min), we observed abrupt transition widths (<10 nm) that were independent of the NW diameter (Figure 4C), as shown by the data in the green shaded regions (labeled I). Second, we observed broadened transition widths (~10−25 nm), as shown by the yellow regions (labeled II), for low pressures with intermediate growth rates and for high pressures with low growth rates. This region also exhibits a diameter dependence (Figure 4C). Third, we observed very broad transitions (>30 nm) and a diameter dependence (Figure 4C) at high NW growth rates for all reactor pressures, corresponding to the red region (labeled III) in Figure 4B. These experimental results were also confirmed by EDS images collected at the lowest pressure, 20 Torr, with the second to lowest and highest NW growth rates (corresponding to regions I and III, respectively). As shown in the fits in Figure 4D, the EDS data yielded transition widths of ~4 and ~30 nm, respectively, under these two conditions.

The three regions observed experimentally can be assigned to different limits of the kinetic analysis (*i.e.*, eqs 6−8). Region I corresponds to synthetic conditions in which evaporation is the dominate term (eq 7), causing abrupt dopant transitions. The low pressures and low growth rates favor efficient evaporation of P from the liquid catalyst. This effect is consistent with the abrupt transitions observed from n-type/intrinsic/n-type NWs grown under high vacuum conditions.[44] Region II corresponds to a regime in which the rate constants for evaporation and crystallization are of similar magnitudes (eq 6). Finally, region III corresponds to a regime in which P evaporation is slow and P crystallization dominates (eq 8), causing substantially broadened transitions. This regime is favored at high NW growth rates (*i.e.*, with high SiH_4 partial pressures) that increase k_{SiC} and ϕ_{Si} while also disfavoring P evaporation because the higher SiH_4 pressure decreases the number of surface sites available for P associative desorption. Using the diameter-dependent data from region III, we can calculate ϕ_{Si} by assuming $\beta \approx 5/3$ and using a modification of eq 8 to account for a non-hemispherical catalyst (see eq S4). The analysis yields a value of $\phi_{Si} = 26 \pm 5\%$, which is in good agreement with previous reports of the equilibrium volume fraction of Si in Au at 420 °C.[26]

The dependence of the dopant transition width on the NW diameter and on the P incorporation and evaporation rate constants is summarized in Figure 5A. Changing the synthetic parameters of VLS NW growth permits a smooth transition between a diameter-dependent transition width consistent with the reservoir effect and a diameter-independent transition width in which the reservoir effect is fully suppressed because of the high rate of P evaporation. Here, we have determined the optimal conditions for abrupt

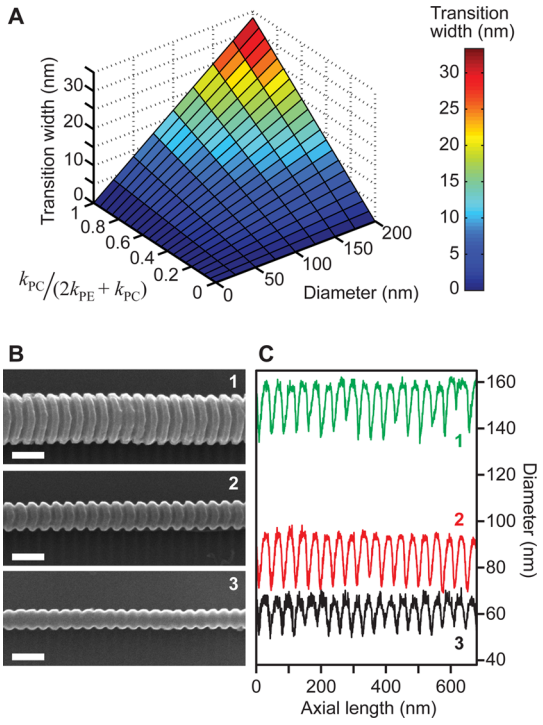

Figure 5. Suppressing the reservoir effect for diameter-independent, high-resolution heterostructures. (A) Plot of the n-type/intrinsic transition width as a function of NW diameter and as a function of the ratio between rate constants for P crystallization and P evaporation, where 0 and 1 correspond to the limits $k_{PE} \gg k_{PC}$ and $k_{PC} \gg k_{PE}$, respectively. (B) SEM images of ENGRAVE NWs created by alternating n-type/intrinsic sections for 6 s each. From top to bottom the NW diameters are (1) ~150 nm, (2) ~100 nm, and (3) ~50 nm; scale bars, 100 nm. (C) Diameter profiles as a function of axial length for NWs 1–3 shown in panel B.

dopant transitions to be low-pressure growth (20 Torr total reactor pressure) with a NW growth rate of ~200 nm/min, corresponding to a SiH_4 partial pressure of 0.4 Torr. Under these conditions, both the dopant transition width and growth rate[28] are independent of the NW diameter. The only apparent disadvantage of these low-growth-rate conditions is increased Au deposition (see Figure S3) on the wire surface,[52] which could potentially be suppressed by addition of HCl to the CVD reactor during VLS growth.[53]

The report of VLS growth conditions that produce abrupt and uniform dopant profiles, as shown here, should assist the development of NW-based technologies. For instance, using the ENGRAVE process,[41] a variety of high-resolution morphological structures can be encoded in NWs with diameters ranging from 50 to 200 nm, as shown in Figure 5B. These NWs were grown with the PH_3 flow profile modulated on or off every 6 s, which corresponds to ~20 nm of NW growth for each section. As demonstrated by the diameter profiles in Figure 5C, the ENGRAVE NWs show no loss in spatial resolution as a function of the wire diameter, which is consistent with full suppression of the reservoir effect.

CONCLUSIONS

By examining the width of P dopant transitions at n-type/intrinsic interfaces as a function of Si NW diameter, growth rate (*i.e.*, SiH_4 partial pressure), and total reactor pressure, we have identified a regime in which the reservoir effect can be fully suppressed to produce transition widths of ~5 nm independent of the NW diameter. Using a detailed kinetic model of NW doping, which includes the processes of P incorporation, evaporation, and crystallization, we have shown that P evaporation plays the primary role in achieving the abrupt interfaces. Our kinetic model can be applied to a wide range of NW materials grown by the VLS process. The results presented here should provide guidelines to develop the synthetic conditions needed to achieve abrupt compositional and morphological transitions in a variety of NW systems.

METHODS

NW Growth. Si NWs were grown in a home-built, hot-wall chemical vapor deposition system using Au catalysts of various diameters (BBI International), silane (SiH_4; Voltaix) as the source of Si, phosphine (PH_3; Voltaix; diluted to 1000 ppm in H_2) as the source of P, and hydrogen (H_2; Matheson TriGas 5N semiconductor grade) as the carrier gas. NWs were grown in a 1 in. tube furnace (Lindberg Blue M) at a temperature of 420 °C with between 0 and 200 sccm of H_2, 0.4–2.0 sccm of SiH_4, 4–20 sccm PH_3, and 20–80 Torr total reactor pressure. All gas flow rates were controlled and measured using mass-flow controllers from MKS Instruments (model P4B). For all NWs in which transition widths were measured, n-type segments were doped at a ratio of 1:100 PH_3:SiH_4. For chemical doping level measurements in Figure 2C, n-type segments were doped at lower levels, as noted in the text.

Etching. NWs were mechanically transferred from the original growth substrate to a 2 mm by 2 mm Si wafer coated with Si_3N_4. The substrate was then immersed in 10% buffered hydrofluoric acid by volume in water (Transene BHF Improved) for 10 s in order to remove any native oxide from the NWs and was subsequently rinsed in water and 2-propanol. The substrate was dipped into a heated 2-propanol solution at 40 °C for ~30 s in order to equilibrate the substrate to the etch temperature. The NWs were then etched in KOH solution (20.0 g of KOH; 80.0 g of water; 20 mL of 2-propanol as top surface layer) at 40 °C for variable times up to 60 s and subsequently quenched in dilute acetic acid (2 mL of glacial acetic acid; 48 mL of water) and rinsed in 2-propanol. The substrate was blown dry with nitrogen to remove excess solvent.

STEM and EDS. Samples for electron microscopy were prepared by mechanical contact-transfer of the NWs directly onto lacey-carbon TEM grids (Ted-Pella #01895). STEM imaging was performed on a Tecnai Osiris operating at 200 kV with a subnanometer probe with a current of 2 nA (spot size 3, 4k extraction voltage). The Osiris is equipped with a Super-X EDS system, which consists of four solid-state detectors built into the objective lens. The maximum peak counts summed from the four detectors were on the order of 45 kcps. The STEM probe was retuned periodically to maintain the integrity of the imaging conditions and beam intensity. Drift-corrected STEM-EDS maps were obtained using the Bruker Esprit software.

Total collection times for each map were 15 min except for chemical doping level data in Figure 2C, which required an averaging time of 3 h. Standardless Cliff−Lorimer quantification was performed on the deconvoluted spectra from subsections of the EDS maps. STEM images were obtained before and after map acquisition to note any change in the sample.

SEM Image Analysis. SEM imaging was performed with an FEI Helios 600 Nanolab dual-beam system with an imaging resolution of less than 5 nm. The diameter profile of each wire was determined from SEM images using home-written MATLAB image analysis software. Diameter profiles were fit to the addition of a Gaussian convoluted with an exponential for the n-type/intrinsic transition and to an error function for the intrinsic/n-type transition. The width of the Gaussian broadening was constrained to be between 2.5 and 3.0 nm during the fit routine. The fit was then converted to doping level using a previously reported exponential fit of etch rate *vs* doping level for Si NWs.[41] The doping level curve was then fit once again to the same functional forms to provide the transition widths reported in the article.

Conflict of Interest: The authors declare no competing financial interest.

Supporting Information Available: Equation used to fit dopant and diameter profiles, determination of the volume fraction of Si in Au, EDS spectrum showing fits for Si and P peaks to determine relative concentration, details of resistivity measurements, full EDS spectrum, and HAADF-STEM image as well as Si, Au, O, and P elemental maps of the n-type/intrinsic/n-type segment in Figure 3A, transition widths at various carrier gas flow rates, and data table of encoded doping level *vs* resistivity and active doping level. This material is available free of charge *via* the Internet at http://pubs.acs.org.

Acknowledgment. This research was primarily supported by the National Science Foundation (NSF) through grant DMR-1308695. C.W.P. acknowledges an NSF graduate research fellowship, and J.R.M. acknowledges NSF support from CHE-1213758 and EPS-1004083. We thank D. Hill, T. Celano, C. Flynn, and S. McCullough for useful discussions and the staff of Chapel Hill Analytical and Nanofabrication Laboratory (CHANL) user facility for assistance with NW imaging.

REFERENCES AND NOTES

1. Lu, W.; Lieber, C. M. Nanoelectronics from the Bottom Up. *Nat. Mater.* **2007**, *6*, 841–850.
2. Zheng, G. F.; Lu, W.; Jin, S.; Lieber, C. M. Synthesis and Fabrication of High-Performance n-Type Silicon Nanowire Transistors. *Adv. Mater.* **2004**, *16*, 1890–1893.
3. Kim, S.-K.; Day, R. W.; Cahoon, J. F.; Kempa, T. J.; Song, K.-D.; Park, H.-G.; Lieber, C. M. Tuning Light Absorption in Core/Shell Silicon Nanowire Photovoltaic Devices through Morphological Design. *Nano Lett.* **2012**, *12*, 4971–4976.
4. Yan, R.; Gargas, D.; Yang, P. Nanowire Photonics. *Nat. Photonics* **2009**, *3*, 569–576.
5. Sirbuly, D. J.; Law, M.; Yan, H.; Yang, P. Semiconductor Nanowires for Subwavelength Photonics Integration. *J. Phys. Chem. B* **2005**, *109*, 15190–15213.
6. Tian, B.; Kempa, T. J.; Lieber, C. M. Single Nanowire Photovoltaics. *Chem. Soc. Rev.* **2009**, *38*, 16–24.
7. Kempa, T. J.; Day, R. W.; Kim, S.-K.; Park, H.-G.; Lieber, C. M. Semiconductor Nanowires: A Platform for Exploring Limits and Concepts for Nano-Enabled Solar Cells. *Energy Environ. Sci.* **2013**, *6*, 719.
8. Dasgupta, N. P.; Yang, P. Semiconductor Nanowires for Photovoltaic and Photoelectrochemical Energy Conversion. *Front. Phys.* **2013**, *9*, 289–302.
9. Garnett, E. C.; Brongersma, M. L.; Cui, Y.; McGehee, M. D. Nanowire Solar Cells. *Annu. Rev. Mater. Res.* **2011**, *41*, 269–295.
10. Thelander, C.; Nilsson, H. a; Jensen, L. E.; Samuelson, L. Nanowire Single-Electron Memory. *Nano Lett.* **2005**, *5*, 635–638.
11. Yang, C.; Zhong, Z.; Lieber, C. M. Encoding Electronic Properties by Synthesis of Axial Modulation-Doped Silicon Nanowires. *Science* **2005**, *310*, 1304–1307.
12. Cohen-Karni, T.; Casanova, D.; Cahoon, J. F.; Qing, Q.; Bell, D. C.; Lieber, C. M. Synthetically Encoded Ultrashort-Channel Nanowire Transistors for Fast, Pointlike Cellular Signal Detection. *Nano Lett.* **2012**, *12*, 2639–2644.
13. Rigutti, L.; Tchernycheva, M.; De Luna Bugallo, A.; Jacopin, G.; Julien, F. H.; Zagonel, L. F.; March, K.; Stephan, O.; Kociak, M.; Songmuang, R. Ultraviolet Photodetector Based on GaN/AlN Quantum Disks in a Single Nanowire. *Nano Lett.* **2010**, *10*, 2939–2943.
14. Jiang, Z.; Qing, Q.; Xie, P.; Gao, R.; Lieber, C. M. Kinked p-n Junction Nanowire Probes for High Spatial Resolution Sensing and Intracellular Recording. *Nano Lett.* **2012**, *12*, 1711–1716.
15. Christesen, J. D.; Zhang, X.; Pinion, C. W.; Celano, T. A.; Flynn, C. J.; Cahoon, J. F. Design Principles for Photovoltaic Devices Based on Si Nanowires with Axial or Radial p−n Junctions. *Nano Lett.* **2012**, *12*, 6024–6029.
16. Kempa, T. J.; Tian, B. Z.; Kim, D. R.; Hu, J. S.; Zheng, X. L.; Lieber, C. M. Single and Tandem Axial p-i-n Nanowire Photovoltaic Devices. *Nano Lett.* **2008**, *8*, 3456–3460.
17. Gudiksen, M. S.; Lauhon, L. J.; Wang, J.; Smith, D. C.; Lieber, C. M. Growth of Nanowire Superlattice Structures for Nanoscale Photonics and Electronics. *Nature* **2002**, *415*, 617–620.
18. Yang, C.; Barrelet, C. J.; Capasso, F.; Lieber, C. M. Single p-Type/Intrinsic/n-Type Silicon Nanowires as Nanoscale Avalanche Photodetectors. *Nano Lett.* **2006**, *6*, 2929–2934.
19. Cui, Y.; Wang, J.; Plissard, S. R.; Cavalli, A.; Vu, T. T. T.; van Veldhoven, R. P. J.; Gao, L.; Trainor, M.; Verheijen, M. a; Haverkort, J. E. M.; *et al.* Efficiency Enhancement of InP Nanowire Solar Cells by Surface Cleaning. *Nano Lett.* **2013**, *13*, 4113–4117.
20. Dey, A. W.; Svensson, J.; Ek, M.; Lind, E.; Thelander, C.; Wernersson, L.-E. Combining Axial and Radial Nanowire Heterostructures: Radial Esaki Diodes and Tunnel Field-Effect Transistors. *Nano Lett.* **2013**, *13*, 5919–59124.
21. Ganjipour, B.; Dey, A.; Borg, B.; Ek, M. High Current Density Esaki Tunnel Diodes Based on GaSb-InAsSb Heterostructure Nanowires. *Nano Lett.* **2011**, *11*, 4222–4226.
22. Guo, W.; Banerjee, A.; Bhattacharya, P.; Ooi, B. S. InGaN/GaN Disk-in-Nanowire White Light Emitting Diodes on (001) Silicon. *Appl. Phys. Lett.* **2011**, *98*, 193102.
23. Nguyen, H. P. T.; Cui, K.; Zhang, S.; Djavid, M.; Korinek, A.; Botton, G. a; Mi, Z. Controlling Electron Overflow in Phosphor-Free InGaN/GaN Nanowire White Light-Emitting Diodes. *Nano Lett.* **2012**, *12*, 1317–1323.
24. Perea, D.; Li, N.; Dickerson, R.; Misra, A.; Picraux, S. Controlling Heterojunction Abruptness in VLS-Grown Semiconductor Nanowires *via* in Situ Catalyst Alloying. *Nano Lett.* **2011**, *11*, 3117–3122.
25. Clark, T. E.; Nimmatoori, P.; Lew, K. K.; Pan, L.; Redwing, J. M.; Dickey, E. C. Diameter Dependent Growth Rate and Interfacial Abruptness in Vapor-Liquid-Solid $Si/Si_{1-x}Ge_x$ Heterostructure Nanowires. *Nano Lett.* **2008**, *8*, 1246–1252.
26. Li, N.; Tan, T. Y.; Gosele, U. Transition Region Width of Nanowire Hetero- and pn-Junctions Grown Using Vapor-Liquid-Solid Processes. *Appl. Phys. A Mater. Sci. Process* **2008**, *90*, 591–596.
27. Givargizov, E. I. Fundamental Aspects of VLS Growth. *J. Cryst. Growth* **1975**, *31*, 20–30.
28. Pinion, C. W.; Nenon, D. P.; Christesen, J. D.; Cahoon, J. F. Identifying Crystallization- and Incorporation-Limited Regimes during Vapor-Liquid-Solid Growth of Si Nanowires. *ACS Nano* **2014**, *8*, 6081–6088.
29. Wen, C. Y.; Tersoff, J.; Reuter, M. C.; Stach, E. A.; Ross, F. M. Step-Flow Kinetics in Nanowire Growth. *Phys. Rev. Lett.* **2010**, *105*, 195502.
30. Persson, A. I.; Larsson, M. W.; Stenström, S.; Ohlsson, B. J.; Samuelson, L.; Wallenberg, L. R. Solid-Phase Diffusion Mechanism for GaAs Nanowire Growth. *Nat. Mater.* **2004**, *3*, 677–681.
31. Wen, C. Y.; Reuter, M. C.; Bruley, J.; Tersoff, J.; Kodambaka, S.; Stach, E. A.; Ross, F. M. Formation of Compositionally Abrupt Axial Heterojunctions in Silicon-Germanium Nanowires. *Science* **2009**, *326*, 1247–1250.

32. Ross, F. M. Controlling Nanowire Structures through Real Time Growth Studies. *Rep. Prog. Phys.* **2010**, *73*, 114501.
33. Dick, K.; Bolinsson, J.; Borg, B.; Johansson, J. Controlling the Abruptness of Axial Heterojunctions in III−V Nanowires: Beyond the Reservoir Effect. *Nano Lett.* **2012**, *12*, 3200–3206.
34. Amit, I.; Givan, U.; Connell, J. G.; Paul, D. F.; Hammond, J. S.; Lauhon, L. J.; Rosenwaks, Y. Spatially Resolved Correlation of Active and Total Doping Concentrations in VLS Grown Nanowires. *Nano Lett.* **2013**, *13*, 2598–2604.
35. Hilse, M.; Ramsteiner, M.; Breuer, S.; Geelhaar, L.; Riechert, H. Incorporation of the Dopants Si and Be into GaAs Nanowires. *Appl. Phys. Lett.* **2010**, *96*, 193104.
36. Wu, Y.; Fan, R.; Yang, P. Block-by-Block Growth of Single-Crystalline Si/SiGe Superlattice Nanowires. *Nano Lett.* **2002**, *2*, 83–86.
37. Amato, M.; Palummo, M.; Rurali, R.; Ossicini, S. Silicon-Germanium Nanowires: Chemistry and Physics in Play, from Basic Principles to Advanced Applications. *Chem. Rev.* **2014**, *114*, 1371–1412.
38. Ohlsson, B.; Björk, M.; Persson, A.; Thelander, C.; Wallenberg, L.; Magnusson, M.; Deppert, K.; Samuelson, L. Growth and Characterization of GaAs and InAs Nano-Whiskers and InAs/GaAs Heterostructures. *Phys. E (Amsterdam, Neth.)* **2002**, *13*, 1126–1130.
39. Hiruma, K.; Yazawa, M.; Katsuyama, T.; Ogawa, K.; Haraguchi, K.; Koguchi, M.; Kakibayashi, H. Growth and Optical Properties of Nanometerscale GaAs and InAs Whiskers. *J. Appl. Phys.* **1995**, *77*, 447–462.
40. Kempa, T. J.; Cahoon, J. F.; Kim, S.-K.; Day, R. W.; Bell, D. C.; Park, H.-G.; Lieber, C. M. Coaxial Multishell Nanowires with High-Quality Electronic Interfaces and Tunable Optical Cavities for Ultrathin Photovoltaics. *Proc. Natl. Acad. Sci. U.S.A.* **2012**, *109*, 1407–1412.
41. Christesen, J. D.; Pinion, C. W.; Grumstrup, E. M.; Papanikolas, J. M.; Cahoon, J. F. Synthetically Encoding 10 nm Morphology in Silicon Nanowires. *Nano Lett.* **2013**, *13*, 6281–6286.
42. Schmid, H.; Björk, M. T.; Knoch, J.; Karg, S.; Riel, H.; Riess, W. Doping Limits of Grown in Situ Doped Silicon Nanowires Using Phosphine. *Nano Lett.* **2009**, *9*, 173–177.
43. Wang, Y.; Lew, K.; Ho, T.; Pan, L.; Novak, S.; Dickey, E.; Redwing, J. M.; Mayer, T. S. Use of Phosphine as an n-Type Dopant Source for Vapor-Liquid-Solid Growth of Silicon Nanowires. *Nano Lett.* **2005**, *5*, 2139–2143.
44. Chou, L.; Filler, M. Engineering Multimodal Localized Surface Plasmon Resonances in Silicon Nanowires. *Angew. Chem., Int. Ed.* **2013**, *52*, 8079–8083.
45. Björk, M.; Schmid, H.; Knoch, J.; Riel, H.; Riess, W. Donor Deactivation in Silicon Nanostructures. *Nat. Nanotechnol.* **2009**, *4*, 103–107.
46. Mueller, D.; Fichtner, W. Highly n-Doped Silicon: Deactivating Defects of Donors. *Phys. Rev. B* **2004**, *70*, 245207.
47. Perea, D. E.; Hemesath, E. R.; Schwalbach, E. J.; Lensch-Falk, J. L.; Voorhees, P. W.; Lauhon, L. J. Direct Measurement of Dopant Distribution in an Individual Vapour-Liquid-Solid Nanowire. *Nat. Nanotechnol.* **2009**, *4*, 315–319.
48. Connell, J. G.; Yoon, K.; Perea, D. E.; Schwalbach, E. J.; Voorhees, P. W.; Lauhon, L. J. Identification of an Intrinsic Source of Doping Inhomogeneity in Vapor-Liquid-Solid-Grown Nanowires. *Nano Lett.* **2013**, *13*, 199–206.
49. Seidel, H.; Csepregi, L.; Heuberger, A.; Baumgartel, H. Anisotropic Etching of Crystalline Silicon in Alkaline-Solutions: II. Influence of Dopants. *J. Electrochem. Soc.* **1990**, *137*, 3626–3632.
50. Wallentin, J.; Borgström, M. T. Doping of Semiconductor Nanowires. *J. Mater. Res.* **2011**, *26*, 2142–2156.
51. The rate constant k_{SiC} as used here is the observed rate constant for Si crystallization in a kinetic analysis that does not explicitly consider the process of Si dissolution from the solid Si NW. As a result, the rate constant must have a weak dependence on supersaturation of the liquid Au-Si droplet and thus on the partial pressure of SiH_4.
52. Madras, P.; Dailey, E.; Drucker, J. Spreading of Liquid AuSi on Vapor-Liquid-Solid-Grown Si Nanowires. *Nano Lett.* **2010**, *10*, 1759–1763.
53. Gentile, P.; Solanki, A.; Pauc, N.; Oehler, F.; Salem, B.; Rosaz, G.; Baron, T.; Den Hertog, M.; Calvo, V. Effect of HCl on the Doping and Shape Control of Silicon Nanowires. *Nanotechnology* **2012**, *23*, 215702.